### **RESEARCH PAPER**



# Design and characterization of solid articulated four axes microrobot for microfactory applications

Ruoshi Zhang 1 • Andriy Sherehiy 1 • Danming Wei 1 • Dan O. Popa 1

Received: 11 November 2018 / Revised: 30 March 2019 / Accepted: 20 May 2019 © Springer-Verlag GmbH Germany, part of Springer Nature 2019

#### **Abstract**

In this paper, we present the design and experimental evaluation of a 3-dimensional microrobot called Solid Articulated Four Axes Microrobot (sAFAM). The sAFAM is fabricated using Microelectromechanical System (MEMS) technology, then assembled to achieve out-of-plane motion and perform micro and nano manipulation tasks relevant to future microfactories such as pick and place and applying controlled forces onto the environment. The paper discusses the design, fabrication and assembly processes for constructing sAFAM. Four in-plane electrothermal actuators drive the end-effector through a complaint mechanical coupling. The microrobot structure was simulated by finite element analysis (FEA), predicting a 13  $\mu$ m × 47  $\mu$ m × 115  $\mu$ m workspace and verifying appropriate concentration of stresses during actuation. The resolution, repeatability, and workspace of the microrobot were then measured experimentally via optical microscopy and laser ranging, indicating a 16  $\mu$ m × 20  $\mu$ m × 118  $\mu$ m dimension workspace. Experiments also indicate that the motion resolution and repeatability of the microrobot varies depending on the location of the end-effector in space, but generally range between 20 nm (minimum) and 150 nm (maximum). With FEA simulation result, the force output of sAFAM falls in the range of tens of micro Newtons. Thus, sAFAM has the potential for future use as an assist micro/nano manipulation tool in the scanning electron microscope (SEM) or in conjunction with an atomic force microscope (AFM).

Keywords Microrobot · Microassembly · Micromanipulation

# 1 Introduction

In the past decades, considerable research efforts have been directed toward making microrobots smaller, smarter and more productive. One of these efforts involves utilizing applied external fields to drive and communicate with microrobots. Amongst external fields, magnetic [1–3] and electrostatic [4–7] fields are the most popular choices for they are well studied and highly efficient. Khamesee et al.

☐ Ruoshi Zhang ruoshi.zhang@louisville.edu

Andriy Sherehiy andriy.sherehiy@louisville.edu

Danming Wei danming.wei@louisville.edu

Dan O. Popa dan.popa@louisville.edu

Published online: 06 June 2019

Department of Electrical and Computer Engineering, University of Louisville, Louisville, KY, USA [8] presented a microrobot system that uses magnetic force to levitate and control the microrobot. They successfully demonstrated that their microrobot was capable of having 3 degrees of freedom (DOF) under remote operation in a closed environment. Later, Diller et al. [9] demonstrated multiple untethered microrobots operated on nonspecific surface and proposed a control method that allow up to three microrobots to be positioned independently. Recently, Hsu et al. [10] demonstrated a 2-D diamagnetically levitated millimeter size robot capable of handling microassembly tasks with long-term open loop submicron precision. Naturally, magnetic field actuation always involves placing certain amounts of permanent or electromagnets into the microrobot body as receptors of the external field to generate locomotion. This requirement limits the applicability and choice of material for these types of microrobots.

As an alternative, microrobots constructed and operated in a manner like Integrated Circuits have also been employed and extensively studied over the last three decades. Fabrication of components using microelectromechanical systems (MEMS) technology opened a new era for micromanipulation and



microrobotics. Yeh et al. [11] demonstrated that hinged structures can be employed to become building element on microrobots. Tests revealed that surface micromachined parts fabricated using Multi-User MEMS Processes (MUMPS) are capable of withstanding payloads in the order of milligrams. Recently, Sarkar et al. [12] commercialized a single-chip atomic force microscope (sc-AFM) with a small footprint and substantial cost reduction that utilize thermal-actuator and piezoresistive sensor to scan target surfaces.

By combining microassembly techniques with silicon parts fabricated by standard CMOS processes, the complexity of the resulting microrobots can be significantly higher than before [13, 14]. Tsui [15] and Geisberger [16] invented a passive snap fastener style MEMS coupling device, widely known as the Zyvex connector, which greatly reduces the effort to perform microassembly tasks by accommodating relatively large micromachining and micromanipulating errors.

Using the modularity of the Zyvex connector, Murthy et al. [17] proposed an articulated four axes microrobot (AFAM) for micro and nano meter sized objects manipulation and probing. In their design, a 1500 µm long robotic arm was coupled to banks of electro-thermal actuators and was capable of generating tens of mN force output and a large end-effector workspace. Using interferometric and Scanning Electron Microscope (SEM) measurements, the AFAM end-effector had a workspace of approximately 50 µm by 50 µm inplane and 75 µm out-of-plane. Despite its large, 3D workspace, the AFAM suffered from operational drawbacks: first, the arm was coupled with the actuators through an epoxied copper cable, which was difficult to assemble; second, assembly errors of the cable and arm stack up and require each AFAM to be individually calibrated after assembly; third, the copper wire's reliability was limited to under one million actuation cycles before failure; and fourth, the end-effector's motion experiences a 70% pitch-yaw axis coupling effect that made its control more difficult.

In this paper we present a new, assembled microrobot, the Solid Articulated Four Axis Microrobot (sAFAM), which improves upon many aspects of the original design. The sAFAM arm assembly consists only of a monolithic micromachined silicon piece with an elastic leaf spring representing an improved motion coupling principle; fabricated by surface micromachining technology and eliminating the epoxied cable. The sAFAM design was first examined using Finite Element Analysis (FEA) simulation, which was validated against experiments to confirm the anticipated workspace, then laser displacement sensor was used to evaluate the resolution and repeatability. Results confirm that the microrobot has a 3D workspace of approximately 16  $\mu$ m  $\times$  20  $\mu$ m  $\times$ 118 µm, a resolution and repeatability below 20 nm in certain regions of its workspace, and a vertical force output of 45μN, making it suitable for future nanoscale work. For instance, with an atomic force microscope (AFM) probe attached to the end-effector, sAFAM can be used as a low-cost precision manipulator or measurement instrument at the nanoscale, such as in studies related to cell adhesion [18], on thin-film coating friction [19], and carbon nanotube adhesion [20].

This paper is organized as follows: Section II describes components of sAFAM and how it is intended to position its tip with four degrees of freedom; Section III gives details of fabrication and assembly processes for the microrobot; in Section IV, a FEA model of the whole microrobot and of its arm spring were simulated to predict performance; then, the workspace measurement to validate FEA results, and resolution and repeatability experimental evaluation are presented in Sections V and VI. Finally, Section VII concludes the paper and discusses future work.

# 2 Physical design of sAFAM

### 2.1 Microrobot components

A fully assembled sAFAM microrobot has three major components: the two MEMS actuator banks, providing in-plane x-y motion; the monolithic arm assembly, which is a single piece of silicon containing heterogenous features to convert in-plane actuator motion onto the end-effector; and a die carrier that interconnects power to the microrobot.

The arm assembly has five components: a cantilever arm, a serpentine spring, a thin beam spring, and the front and rear Zyvex stands. Figure 1a depicts the arm assembly design with typical dimensions in microns and it is fabricated on the same silicon wafer as the rest of the parts. The arm assembly has a 100 µm tall, 2.954 mm long cantilever beam with a round tip, which allows for future mounting of tools such as an AFM probe. The fixed end of the cantilever beam is connected with two springs: the serpentineshaped spring containing 8 turns with 20 µm radius allows deflection on both lateral (X and Y axes) and axial (Z axis) directions, and connects the arm with the front Zyvex stand; a thin-beam spring with dimensions of 10 µm width and 2487 µm length, provides an axial stiffness greater than its lateral stiffness to transmit pushing and pulling forces from the actuator banks to the end-effector.

The Zyvex connector system provides a means to assemble the arm piece to the MEMS X-Y stages (Fig. 1b) and further transmit motion from the actuator to the end-effector. The connector system's major two components are shown in Fig. 1c: the plug and the socket. During assembly, a jammer opens the claws marked by red along the direction indicated by arrow, and the blue claws of the socket opens then interlock to each other [15, 16]. The detailed design and analysis of these connectors have been studied extensively in the past and shown to be effective out-of-plane couplers for micromechanisms and micromirrors [13–17].



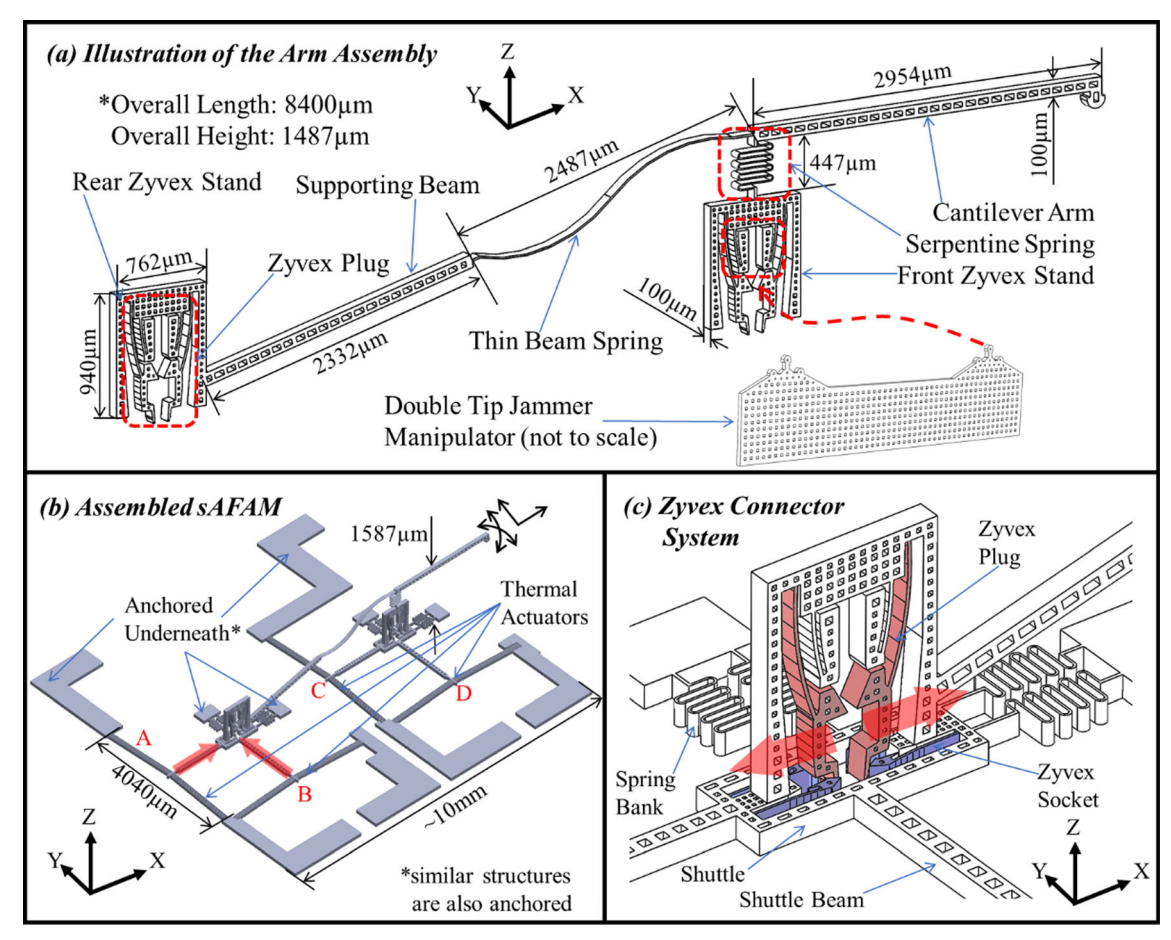


Fig. 1 (a) Side view of the arm assembly with dimension and naming of each critical part. (b) Illustration of a fully assembled sAFAM microrobot, with name of the actuators marked red. (c) Zoom-in view of the rear Zyvex connector

To generate motion, the sAFAM uses two in-plane actuator banks consisting of coupled X-Y micromechanisms shown in Fig. 1b. The two in-plane X-Y stages are anchored on the substrate by a 2 µm thick buried-oxide (BOX) layer under the electrodes. On each X-Y stage, three anchors are coated with gold contacts and two pairs of thermal actuators are fabricated between them. The width of the thin beams of the thermal actuator is 10 µm and they form an 86.57° angle with the anchor. A shuttle with a Zyvex socket is located at the center of the X-Y stage, which connects to the thermal actuators through a shuttle beam. On the other side of the shuttle, two pairs of anchored serpentine springs support the shuttle by lifting it and preventing it from touching the substrate. The two X-Y stages are identical in shape and orientation, and their shuttles are aligned so the arm assembly can be mounted onto them. Since the thermal actuators can only be actuated toward their bending direction, they must be arranged in the same orientation to achieve 4 DOF. The choice of these geometric parameters is discussed in more detail in [17].

Each X-Y stage has two thermal actuators connected to the center shuttle. When one actuator is engaged, the shuttle moves along the actuation direction, shown as the red arrows in Fig. 1b, while dragged by the other pair of the actuator. Then this motion is coupled to the arm assembly through the Zyvex stands. By engaging different actuators, a different motion pattern on the arm assembly is achieved. To clarify discussion, each actuator is named as A, B, C and D, as indicated in Fig. 1b.

sAFAM has 4 DOFs, as it enables tip motion in yaw, pitch, translational X and Y directions, as described in the coordinate system (XYZ reference frame) defined in Fig. 1b. The pitch motion with an axis of rotation aligned with the Y direction generates coupled tip displacement in the X and Z direction. The yaw motion has its axis of rotation aligned with the Z direction generates coupled tip displacement in the X and Y direction. Pitch and yaw motion can be realized thanks to the serpentine spring supporting cantilever arm depicted in Fig. 1a, which acts as a 2-dimensional rotation joint. The thin beam spring can be modeled as a cantilever that does not compress or elongate easily but is able to bend laterally by external force. The pitch motion is generated by engaging either actuator A or C. When A is engaged, the distance between the two Zyvex stands becomes smaller, and the thin beam spring gives the cantilever arm a forward movement and the end-effector pitches towards substrate, e.g. in the –Z direction. When C is engaged, it similarly generates a pitch



motion while the end-effector tilts upward in the +Z direction. When actuators B or D are powered, the serpentine spring serves as a pivot, allowing the thin-beam to drive the end-effector towards -Y or + Y direction in XY plane as the end-effector yaws. Finally, to generate a translational forward motion in the +X direction, actuators A and C are engaged simultaneously. Similarly, when actuator B and D are engaged at the same time, the end-effector moves towards +Y direction to generate lateral translational motion. A detailed kinematic model for AFAM, confirming its 4-DOF positioning capability was studied by Z. Yang et al. in [21].

### 2.2 Assembly methodology

The construction process of sAFAM undergoes two major steps: preliminary part assembly and permanent attachment using ultra-violet curable epoxy adhesive. To successfully assemble the arm assembly into the two in-plane X-Y stages on the substrate, a double tip jammer microgripper is used as depicted in Fig. 1(a). It includes two round tips of 75  $\mu$ m diameter and a rectangle body. The distance between the two jammer tips is 5.050 mm, which is the same as the distance between the two Zyvex stands on the arm assembly and the distance between the two Zyvex sockets on the X-Y stage banks.

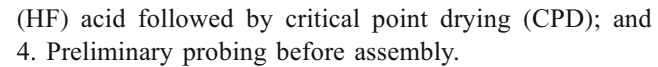
With the help of the jammer manipulator, the arm assembly is picked up, reoriented and aligned with the assembly site (the Zyvex socket) on the substrate using controlled robotic positioning. Once aligned to desired socket location, the jammer performs a precise push-down motion and snaps the arm into the substrate: the red dashed arrow in Fig. 1a shows the right jammer tip pairs with the front Zyvex plug. During part pickup, the tip inserts into the upper half of the Zyvex plug; after alignment, the jammer pushes down and opens the lower part of the plug and interlocks the Zyvex connector system.

### 3 Fabrication and assembly

The fabrication and assembly process of sAFAM, and its associated robotic hardware is described in this Section.

### 3.1 Fabrication

The sAFAM was fabricated on a Silicon on Insulator (SOI) wafer by MEMS process at the Micro/Nano Technology Center at University of Louisville. The SOI wafer has the following specification: 100  $\mu$ m device layer, N type (100), 0.01–0.02  $\Omega$ -cm resistivity, 2  $\mu$ m BOX and 500  $\mu$ m handle layer. Four major fabrication steps are involved: 1. Metal deposition; 2. Deep reactive ion etching (DRIE); 3. MEMS part releasing with hydrofluoric



Metal deposition process deposits a thick layer of gold (above 300 nm) by PVD-75 thin film deposition system (Kurt J. Lesker Company, PA, USA) for 4 min under 300W DC power, which provides electrodes for final wire bonding to a package. To boost Au - Si bounding, an intermediate layer of chrome was also deposited for 2 min before depositing gold. Metal patterning was done by subtractive process: a light-field mask imposes the desired pattern onto positive photoresist, then baked and etched by gold and chromium etch under designated chemical benches. Another layer of photoresist SPR220-3.0 (MicroChem Corp., MA, USA) was deposited and patterned with a dark-field mask featuring DRIE patterns and fully covers the metal that been deposited. The photoresist used in this step must have enough thickness to withstand DRIE process to ensure the integrity of fine micromachined silicon features. And an extended baking procedure was preferred to drive the solvent out of photoresist, hence strengthening it.

DRIE (SPTS Technologies Ltd., Newport, UK) was performed in a timed and inspected manner: the etching rate was characterized by measuring 15 min etching depth, and the finial etching time was based on that number. Inspection on fine features such as releasing holes was needed to guarantee a successful micromachining.

Releasing with 49% hydrofluoric acid was performed after dicing the wafer by immersing each die into the acid. The releasing time for each die depends on their maximum undercut sizes, which ranges from 20 to 30 min. After release, samples are preserved in deionized (DI) water and immediately transferred to a critical point dryer (CPD) to remove liquid to prevent adhesion.

### 3.2 Assembly

Assembly of the sAFAM was performed with NEXUS [22] microassembly station, shown in Fig. 2. This system consists

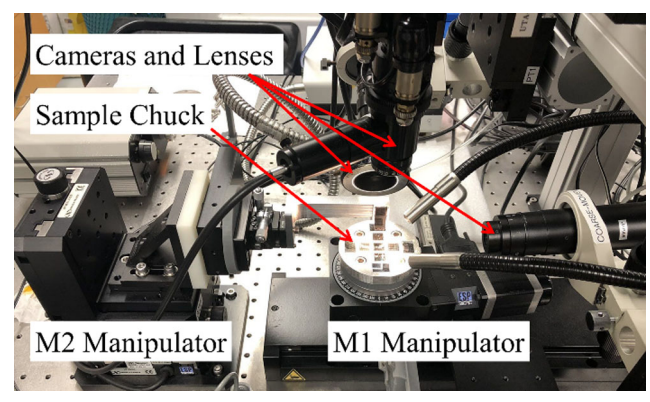


Fig. 2 NEXUS microassembly station:  $M_1$  and  $M_2$  manipulators; top camera: EO-1312C, side camera: EO-6412C



of two cameras with high, adjustable (2x-10x) power optics, one mounted at the top (EO-1312C, Edmund Optics Inc., Barrington NJ, USA) provides a top-down view; the other was mounted at side (EO-6412C) perpendicular to the top, providing a horizontal view. The cameras can track the jammer end-effector motion during rotations, de-tethering and assembly operations. The sample chuck was mounted on the base manipulator M<sub>1</sub>, and it can hold five dies at the same time and has vacuum channels to securely fix each die. The two computer-controlled micromanipulators, M<sub>1</sub> and M<sub>2</sub>, provide a total of 9 degrees of freedom. M<sub>1</sub> (consists of: ILS250CC, 443 Series and URS75BPP, all from Newport Corporation Irvine, CA, USA) provides motorized X-Y translation and rotation to the sample chuck; M2 (VP-25XL-XYZR and PR50CC, both from Newport Corporation Irvine, CA, USA) consists of a motorized X-Y-Z translation stage and a rotation stage, and a mini manual X-Y stage mounted on the rotation stage to adapt the end-effector, totally providing 6 degrees of freedom. An exchangeable end-effector was connected to the manual stage by magnetic connection. Illumination was provided with two fiber lamps with adjustable angle and brightness.

The assembly process starts by fixing the double tip jammer onto the  $M_2$ 's end-effector of the microassembly station using Super 77 adhesive (3 M, MN, USA). Next, we orient the jammer at a 90-degree angle to the substrate, allowing the tips to face downward. With the help of top camera, the operator roughly translates the jammer to the arm assembly, then fine tunes the orientation of the jammer to align with the tethers that hold the arm assembly in place. After breaking the MEMS tethers, the arm assembly was free to be picked up by the jammer through the snap-fastener, which is compliant and allows for alignment error mitigation in excess of 5  $\mu$ m [15, 16]. After the arm pick-up, the end-effector rotates 90 degrees again and align the arm assembly with the Zyvex socket, then insert the arm assembly into the Zyvex sockets on the MEMS X-Y stages.

Although the snap-fasteners are good temporary fixtures, they will not be able to withstand significant forces and torques without disassembly. As a result, the arm assembly was fixed onto the actuator banks using UV curable epoxy (Bondic®, Aurora, ON L4G 3 V5, CA). A small amount of UV adhesive was brushed with a single optical fiber at critical locations of the snap fasteners after pre-assembly. A UV flash light was then used to cure the epoxy immediately after dispensing. Figure 3 depicts a fully assembled and packaged sAFAM arm, which is now ready for the actuation cycling.



Fig. 3 Side view of the assembled sAFAM arm

### 4 Finite element analysis of microrobot

In order to analyze and verify the functionality of sAFAM, a finite element analysis (FEA) was carried out using ANSYS®. The sAFAM photolithography mask was designed in Tanner L-EDIT®, then exported into a .dxf file. 3D models of microrobot components were then extruded in SolidWorks® by introducing corresponding .dxf files. Finally, a 3D solid model in .sldasm format was imported into ANSYS® for FEA simulation.

### 4.1 The experiment assisted simulation method

The performance of the MEMS X-Y stage was previously studied in detail in numerous articles [22–25], which describe both its displacement and force output. The geometry of the thermal-actuator banks of sAFAM is shown in Fig. 1b. The five Chevron beams have a length of 2004  $\mu m$ , width of 12  $\mu m$ , and thickness of 100  $\mu m$ . They are spaced 18  $\mu m$  apart. The length of the shuttle beam is 1790  $\mu m$ . As reported in [17], this actuator bank is capable of generating 50mN of force and 48  $\mu m$  of displacement if not coupled with in-plane serpentine springs. Furthermore, the X and Y axes are stiffened by adding in-plane spring banks with a torsional stiffness of 0.12 Nm/rad and 0.26 Nm/rad for in-plane and out-of-plane motions, respectively.

In general, electrothermal actuator simulation requires accurate information about the boundary conditions, such as substrate temperature, environmental air temperature, actuation voltage etc. In addition, a coupled thermal and electrical analysis needs to be undertaken. In this work, we conducted experimental testing to obtain ranges for X-Y stage actuation displacement to avoid complex coupled simulations. Specifically, after fabrication and packaging, a range of pulse width modulated voltages from a 25V power supply was applied onto the electrodes of the thermal-actuators, while displacement measurements of the Zyvex socket were recorded with a camera and microscopic lens set. Resulting thermal actuator displacement in both X and Y directions varied from 0 to 20 μm. However, for some actuators when the input voltage passes 15 V, the actuator beams start to suffer buckling effects and the displacement of the center shuttle drops, which ANSYS simulation cannot cover. Therefore, the displacement inputs used in the simulation for each actuator was below the buckling threshold. A comparison of the resulting simulation and experimental results obtained are discussed in detail in section V of the paper.

# 4.2 Stiffness analysis of the thin beam spring and the serpentine spring

As stated in Section II-A, the two springs translate the in-plane motion onto the pitch and yaw motion of the cantilever arm.



This phenomenon is confirmed with the help of ANSYS simulation. To observe the pitch motion, actuator A was activated with  $10~\mu m$  of displacement as simulation input; while the yaw motion was observed with  $10~\mu m$  displacement input on actuator B. The simulation result is shown in Fig. 4, which depicts the deformation on the joint of the two springs: the wireframe indicates the undeformed shape and the solid colored indicates the deformed shape.

The magnitude of pitch and yaw depends on the design parameters of the two springs. Design parameters include the shape of the springs represented by the length of the springs, the radii of turns, and the separation distance between Zyvex connectors. To understand the effect of various geometric parameters of these springs, we carried out FEA simulations by assigning the "Fixed Support" boundary conditions and applying external forces to indicated regions shown in Fig. 5. With this simulation data, we calculated stiffness coefficients along X, Y and Z directions, and selected geometric parameters such that maximize the pitch and yaw range of motion.

The results shown in Table 1 correspond to the geometric parameters of the design shown in Fig. 1. The axial stiffness of the thin beam in the X direction was 76.68 N/m, which was significantly larger than the stiffness of the serpentine spring in the X direction (10.04 N/m). This value was comparable to the stiffness of the serpentine spring in the Z direction (66.34 N/m), creating a large pitch motion for the cantilever arm shown in Fig. 4a. On the other hand, the yaw motion of the cantilever is due to the Y direction stiffness of the serpentine spring (26.03 N/m) which is larger than Y direction stiffness of the thin beam spring (5.56 N/m), so that when actuator B engages, the serpentine spring pivots rather than bent towards Y direction. When designing this arm mechanism, there will be trade-offs between the range of motion and the force output of the end-effector. In our design we emphasized maximizing the range of motion, rather than the amount of endeffector force. Although the in-plane thermal actuators can generate mN level forces, due to the low stiffness of the thin beam spring, sAFAM's end-effector transmits µN level forces to its end-effector. The force output of this design at maximum actuator deflections was 55µN in the pitch direction, 120µN in the yaw direction and 1mN in X translational direction.

# 4.3 Stress analysis of the arm assembly

Stress distribution is an essential factor in the reliability of the sAFAM. Silicon can withstand 7GPa of stress measured by Von Mises Method [26]. With maximum actuator displacement as boundary condition added to the structure, the maximum stress point of the whole structure was found at the supporting springs on the in-plane X-Y stage of 139 MPa, while the highest stress reading of 49 MPa was found on the arm assembly of the thin beam spring when actuator B was engaged. Both readings are much smaller than 7GPa. These results suggest that the considered geometry of the sAFAM's structure might be able to withstand a significant number of actuation cycles, while the exact number of actuations needs to be confirmed experimentally.

# 4.4 Simulation of microrobot tip displacement

The goal of this simulation is to determine the relationship between actuator displacement and sAFAM's tip motion. Red arrows in Fig. 1b denote the direction of displacement input on the thermal actuators in the simulation. In this model, as in the case of the assembled structure (Fig. 1b), the displacement inputs on each actuator are denoted as A, B, C and D.

In order to optimize the structural simulation, the multizone meshing method was used to generate an even mesh across the whole robot (76,388 elements, above 91.5% elements have skewness below 0.5) with refined element size of 20  $\mu$ m at critical locations such as the thermal actuator beams, the serpentine spring and the thin beam spring. Although the silicon lattice orientation affects Young's modulus [27, 28], an average value of 160 Pa was chosen in this simulation.

To maximize accuracy, the simulation was assisted with the results form displacement experiments with an assembled sAFAM structure. Two actuation voltages that under buckling threshold were selected to power each thermal actuator, with corresponding shuttle displacement been recorded by the top camera. These displacement data were then inserted into ANSYS model to evaluate the end-effector's displacement. For example, the pitch motion simulation was obtained by

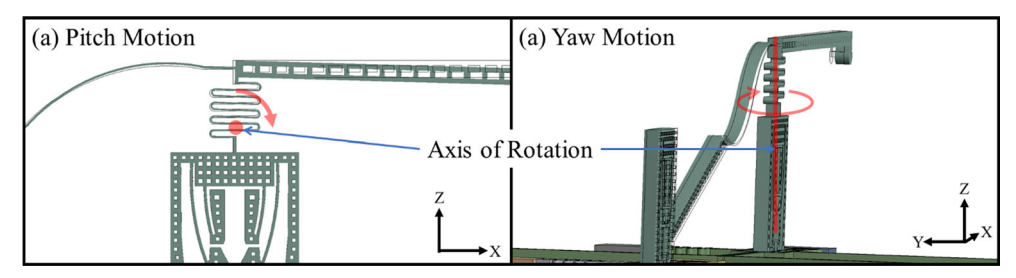
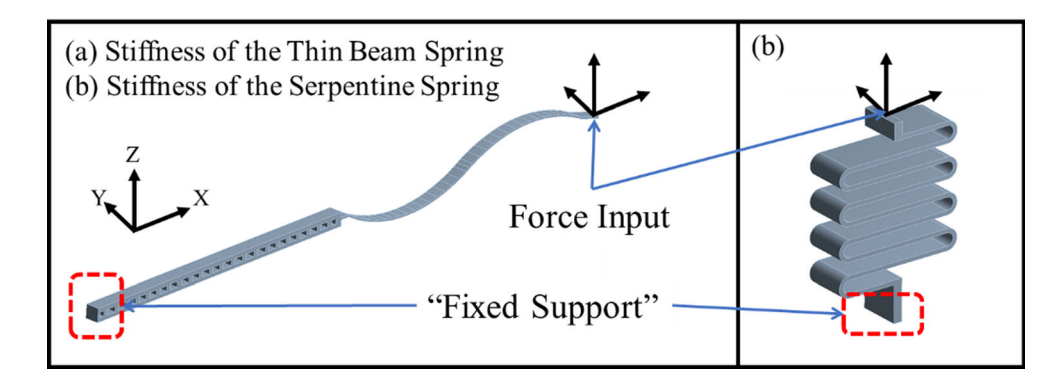


**Fig. 4** Original position (wireframe) vs. actuated position (solid colored). (a) When actuator A is engaged with 10 μm displacement, the axis of rotation is along Y axis. The cantilever arm pitches down. (b) When

actuator B is engaged with 10  $\mu m$  displacement, the axis of rotation is along Z axis. The cantilever arm yaws. The scale factor is set to 2 for demonstration purpose



**Fig. 5** ANSYS simulation setup to study the stiffness of the thin beam spring and the serpentine spring



providing X direction input of 10 V on either actuator A or C, then measuring displacement along the Z direction as  $-43.6~\mu m$  and  $44.4~\mu m$  respectively. The smaller displacement along X and Y directions is due to the motion coupling effect of the structure. Furthermore, yaw motion is generated by either engaging actuator B or D along the Y direction. Forward motion (+X) is generated by engaging A and C together and lateral (-Y) motion is generated by engaging B and D simultaneously. Table 2 rows 1 through 4 show the resulting simulated end-effector displacement along X, Y and Z corresponding to those combinations of actuator inputs that create displacement primarily along those directions. The simulation shows that the end-effector is expected to translate approximately 13  $\mu$ m on X-axis, yaws 47  $\mu$ m on Y-axis and pitches 115  $\mu$ m on Z-axis.

## 5 Experimental results: microrobot workspace

### 5.1 FEA model validation using optical microscopy

The FEA simulation was conducted with thermal actuator displacement input determined from the experiments with a fully assembled sAFAM. To carry out these experiments, a custom made electronic PWM MEMS driver with LabVIEW® interface was developed to apply controlled voltages on the four actuator banks of the microrobot. A motor controller L298 N (STMicroelectronics, Geneva, Switzerland) module was used to drive the thermal actuators by PWM signals generated from the interface. The power module was a voltage boost converter features XL6009 (XLSEMI Inc., Shanghai, China) chip, that can boost 12 VDC to 25VDC. A

camera (EO-1312C) with zoomable lens was placed on top of the sAFAM to observe both the thermal actuator and the endeffector displacement on X and Y direction; the side camera (EO-6412C) was placed perpendicular to the top camera, which focused on the end-effector to observe the pitch motion or Z direction displacement.

Each thermal actuator's static actuation displacement was individually recorded by the top zoom camera microscope under two actuation conditions of 10 V and 15 V, corresponding to 44% and 61% of PWM duty cycle, while the rest of the actuators were not powered. Resting and actuated positions of both center shuttle and the end-effector were recorded with blue lines in the captured pictures, as shown in Fig. 6. The pixel to length ratio was then calibrated and displacement was acquired by measuring the pixel distance from captured frames. Figure 6 shows an example of displacement measurement for thermal actuator from top (a) and end-effector from side (b) and top (c).

The displacement data was imported into the FEA model to obtain simulated tip displacements for validation that are shown in Table 2 rows 1 to 4. Table 2 rows 5 to 7 summarizes the measured tip displacements. The experimental results and the simulations agree for the sAFAM tip displacement in X and Y directions, but a much larger discrepancy for Z direction, even though the trends are the same. The disagreement could be because of etching errors in the two spring geometries. Another cause could have been due to the non-rigid Zyvex connector assembly, which can reduce the transmission effect of forces from the actuators to the end-effector. As a result, the coupling of the sAFAM's arm with actuators is less responsive than indicated in simulation. Nevertheless, the experimental results show that significant displacement in the Z

**Table 1** Simulation result of stiffness for the thin beam spring and the serpentine spring

	Thin Bear	n Spring		Serpentine Spring			
Deformation & Force Direction	X	Y	Z	X	Y	Z	
Force Input (µN)	10	10	10	50	50	50	
Deformation	0.1304	1.7972	21.2110	4.9792	1.9208	0.7537	
Stiffness (N/m)	76.68	5.56	0.47	10.04	26.03	66.34	



**Table 2** ANSYS simulation result depicting sAFAM tip displacements in X, Y and Z direction as a function of actuator input voltages (under row X, Y and Z), and corresponding experimental measurement results using

optical microscopy (0.535 μm/pixel for X and Y direction, 0.503 μm/pixel on Z direction. Under row X', Y' and Z')

Axis	A (10 V)	A (15 V)	B (10 V)	B (15 V)	C (10 V)	C (15 V)	D (10 V)	D (15 V)	AC (10 V)	AC (15 V)	BD (10 V)	BD (15 V)
Input Displ.	9.7	13.4	9.7	11.8	9.6	11.8	9	9	9.7, 9.6	13.4, 11.8	9.7, 9	11.8, 9
X (μm)	7.0	9.7	0.5	0.6	2.9	3.5	-0.3	-0.3	9.6	12.9	-0.3	-0.2
$Y (\mu m)$	3.0	4.0	-21.6	-26.3	-5.3	-6.5	20.7	20.7	-2.3	-2.3	-1.1	-5.8
$Z(\mu m)$	-43.6	-60.2	0.3	0.3	44.4	54.7	-8.2	-8.2	0.1	-7.2	-8.6	-8.6
X' (μm)	7	12	0	0	2	2	0	0	9	14.5	0	0
$Y'(\mu m)$	0	0	-6	-6	-6	-6	14	14	0	0	10	11
$Z'\left(\mu m\right)$	-12	-26	0	0	13	23	0	0	6	-6	0	0

direction can be achieved if actuators A and C are energized to 15 V, as shown in Table 2.

### 5.2 Workspace measurement of sAFAM

A feature recognition LabVIEW® VI was implemented to automate the end-effector workspace characterization using the top and side-view microscopes. Two recognizable features from the end-effector were selected to serve as the top and side visual matching templates as shown in Fig. 6b, c: the half circle feature on the end-effector for the side, and a bright edge of the end-effector that has clear visibility as seen from the top. The LabVIEW® PWM electronics interface was then combined with feature recognition VI to form an automated workspace measurement VI to determining the workspace of sAFAM. The VI cycles through four actuation voltages with PWM duty cycles of 0%, 31%, 63% and 98% applied to actuators A, B, C, D of the sAFAM to generate a total of  $4^4 = 256$  sets of X-Y-Z coordinate measurements of the endeffector position. These 256 data points were recorded from both top and side view cameras as pixel count, and micronpixel relation was estimated from actual measurements of similar features against a known etalon length to 0.546 µm/pixel for top view camera and 0.500 µm/pixel for side view camera.

Then, a MATLAB® script was written to process and display the end-effector's displacement, which is calculated by subtracting the resting position from actuated positions and converting the pixel count to  $\mu m$ . Eventually, a

point-cloud representation of the sAFAM's workspace was visualized in Fig. 7. The dimension of the workspace is bound by a 3D parallelepiped with approximate dimensions of  $16 \ \mu m \times 20 \ \mu m \times 118 \ \mu m$ . The bounding box is an over estimate of the actual workspace of the end-effector, since most of the point clouds concentrates at the center and upper half of the boundary.

# 6 Experimental results: microrobot resolution and repeatability

Important specification of the tools for micro/nano manipulation applications are precision metrics, such as resolution, and repeatability.

To evaluate resolution and repeatability of the sAFAM, a series of measurements were conducted using the experimental setup shown in Fig. 8a, b. Precise measurements of the sAFAM's tip were conducted with the help of the laser displacement sensor - LK-H008 (Keyence Corporation of America, NJ, USA) with 10 nm measurement resolution. A packaged sAFAM was mounted on the X-Y stage (manual/motorized) and a microscope with camera (PL-B742F, Pixelink, ON, CA) with the top or side view, allowing precise alignment of the LK-H008 and sAFAM's arm. While the LK-H008 was attached to a separate manual X-Y-Z stage independent from the sample stage.

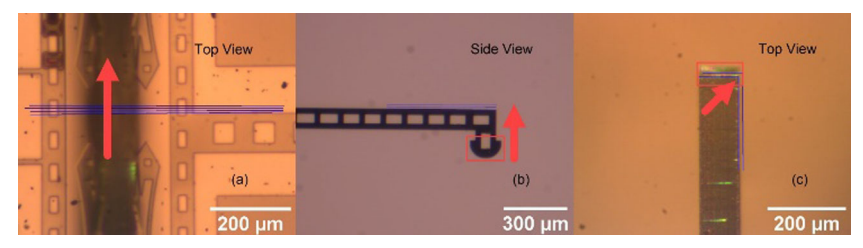


**Fig. 6** (a) Front actuator displacement when actuator C was powered. (b) Side view of the end-effector displacement when C was powered. (c) Top view of the end-effector displacement when C was powered. The red box

indicates the vision matching template in (b) and (c). Blue lines mark displacement in (a)-(c)



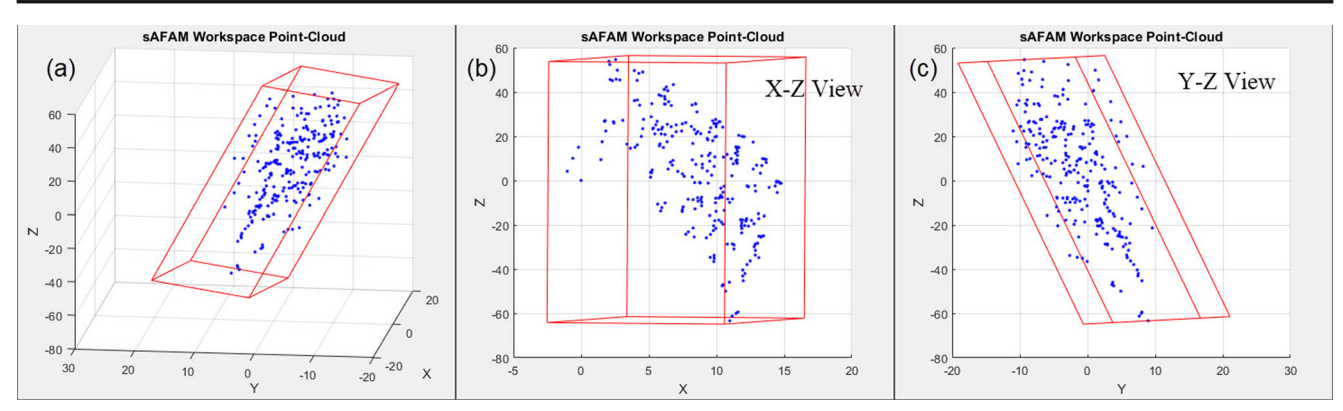
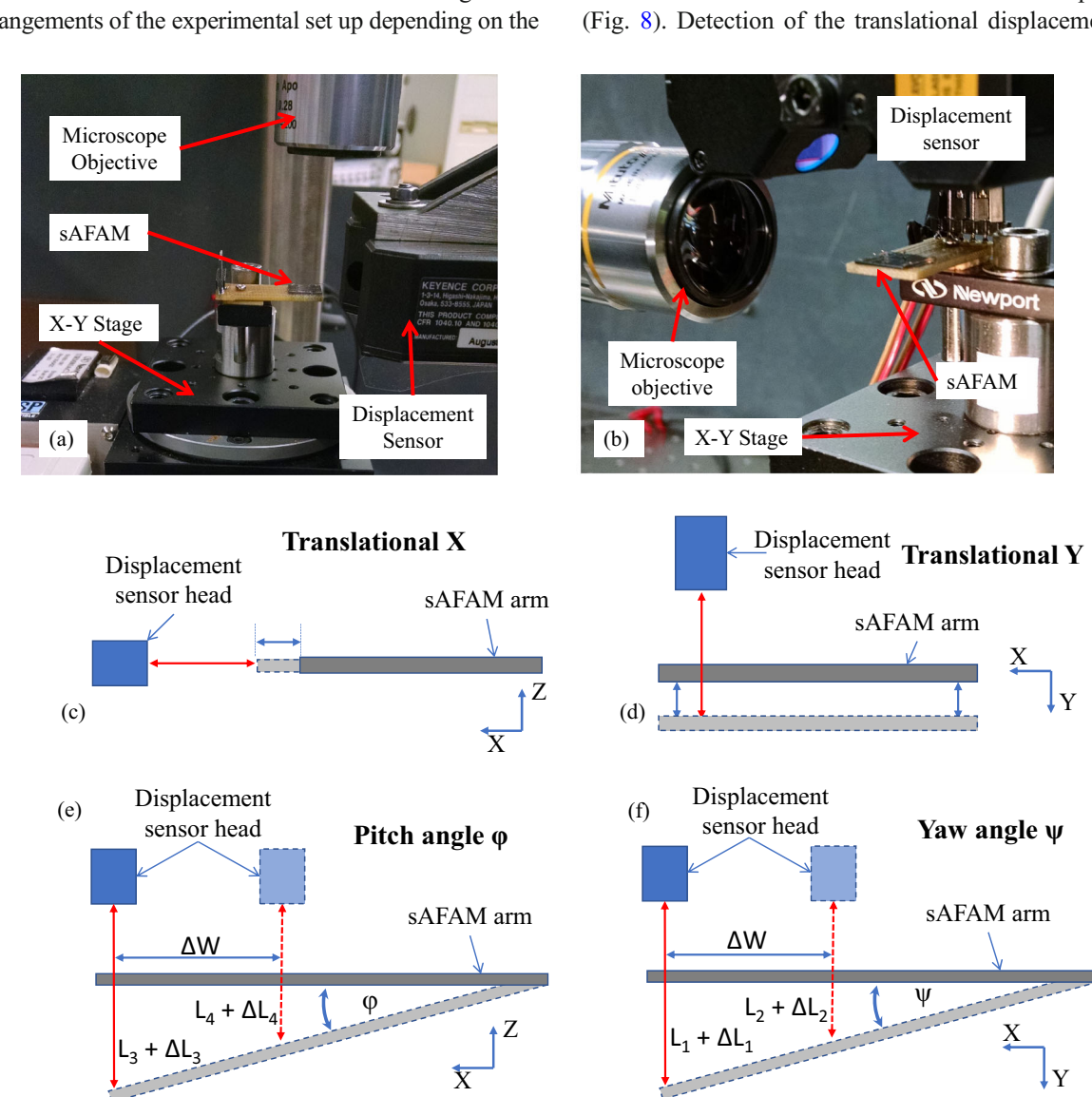


Fig. 7 Measured sAFAM workspace (a) iso view, (b) X-Z plane projection (c) X-Y plane projection

All measurements were taken with one sensor using different arrangements of the experimental set up depending on the

considered direction of the sAFAM's arm displacement (Fig. 8). Detection of the translational displacement along



**Fig. 8** Image of two different arrangements of the experimental set up for the measurements of: (a) translational motion in X direction, the displacement sensor faces the end-effector tip and the camera observes from atop, and (b) pitch angle  $(\phi)$  measurement, the displacement sensor

mounts atop, and the camera observes from side. Schematics of 4 different arrangements for the measurements of: (c) translational displacement in X direction, (d) transl. displ. in Y direction, (e) pitch angle  $(\phi)$ , (f) yaw angle  $(\psi)$ 



the X and Y axes (prismatic DOF (X, Y), Fig. 8c, d), required that the measurements (with the help of displacement sensor) be taken along the corresponding directions of the arm's motion (X or Y). Two series of the displacement measurements at two different positions relative to the sAFAMS's arm (Fig. 8e, f) were conducted to measure revolute DOF (pitch angle  $(\phi)$  – XZ plane, yaw angle  $(\psi)$  – XY plane). In the case of yaw angle, the first series of measurements was taken at one position (L<sub>1</sub>), and after that, the sensor was moved along sAFAM's arm axis to a different position (L<sub>2</sub>) in the same plane of revolution (XY). The second series of measurements was taken, for the respective value of the actuating voltage (Fig. 8f). Using the collected data, yaw and pitch angles could be calculated from the following formula [14]:

$$\psi \ or \ \varphi = \arctan\left(\frac{\Delta L_1 - \Delta L_2}{\Delta W}\right), \tag{1}$$

Where  $\Delta W = W_1 - W_2$ , is the separation distance between two different positions of the sensor, whereas  $\Delta L_1$  and  $\Delta L_2$ represent incremental displacement detected by the sensor for the corresponding positions,  $L_1$  and  $L_2$ . Section V describes the displacement measurements for the detection of the translational motion in X direction. To achieve this motion the pair of A + C actuators were used for the X direction, and B and D were used for the Y direction. Actuator A was used in case of the pitch angle  $\varphi$ , and actuator B for yaw angle  $\psi$ . All the experiments were conducted under similar conditions, and actuation was realized using constant voltage or modulated at 4 Hz (50%) duty cycle). The experiment used a DC power supply (6622A, Hewlett Packard, Palo Alto, CA), a function generator (33,120, Agilent/Hewlett Packard, Palo Alto, CA) and a power amplifier (2348, TEGAM Inc., OH, USA). Displacement measurements were done at 200 µs sampling rate with LK-H008 displacement sensor, which allows collection of at least 1000 data points during actuation with input signal at 4 Hz.

### **6.1 Resolution measurements**

Resolution is defined as the smallest increment of movement that sAFAM's arm can make. To determine such minimal measurable deflection, a series of experiments were conducted with the help of the displacement sensor, where the voltage input to the actuators was incremented with the step size between 5 mV and 200 mV for the given displacement of the end-effector, for each of the 4 degrees of freedom. Based on the sAFAM's arm response, it was determined that the values of the minimum voltage increment varied depending on the actuator, but the overall input needed induce detectable deflection of the robot's arm lay in the range of 50 mv – 200 mV. Such minimum increment value varied depending on the actuator, and the amount of actuation voltage needed to induce specific displacement of the arm.

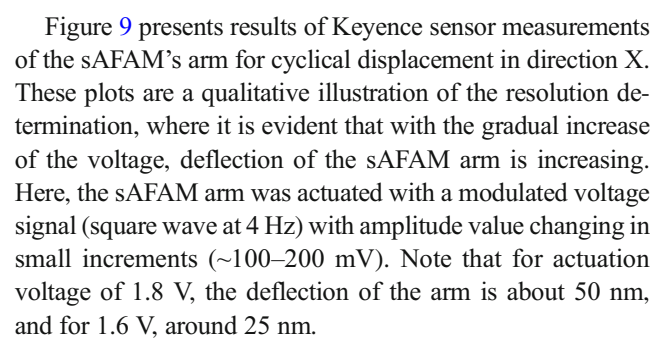
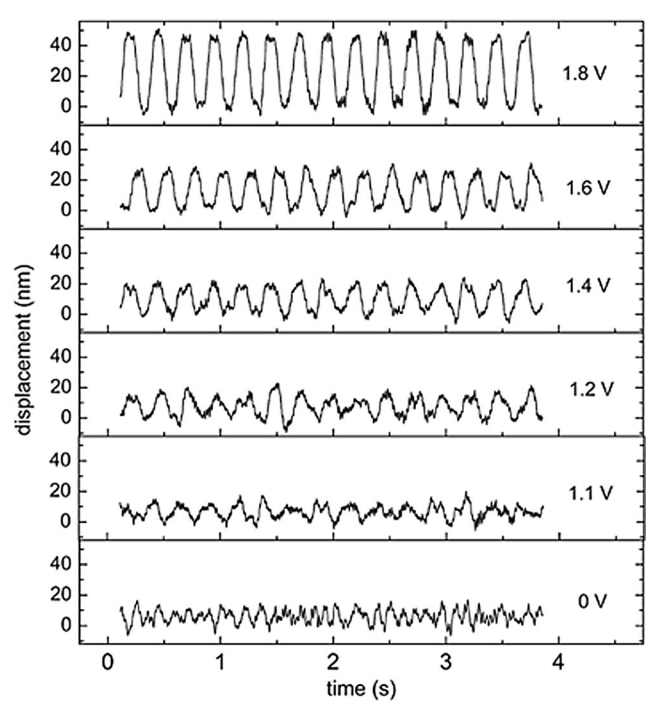


Figure 10 demonstrates variations of the resolution depending on the magnitude of sAFAM arm deflection. Resolution along the X and Y axes range between 20 and 120 nm, and between 0.15-0.45 mrad for the yaw and pitch angles. Resolution values for  $\varphi$  and  $\psi$  were calculated with the help of Eq. 1. As can be seen from Fig. 10, the resolution change for X and Y with increase of the displacement, follows a similar trend: A higher resolution and larger relative variation is achieved for smaller values of actuator inputs (X, Y < 6 μm). For displacements above 6 μm, there is a noticeable plateau where resolution remains relatively steady in a range between 60 and 80 nm. As reported in [17], such behavior could be attributed to the nonlinear displacement and stiffness characteristics of the electrothermal MEMS actuator. Total variations in resolution for X and Y are 60 nm and 100 nm respectively. It should be noted that while in previous studies of the original AFAM's [17], resolution was lower for smaller deflections and improved with larger actuator inputs, we observed an opposite trend in this case. This discrepancy is likely



**Fig. 9** Displacement of the sAFAM arm in the X direction (translation) as a function of time and actuation voltage



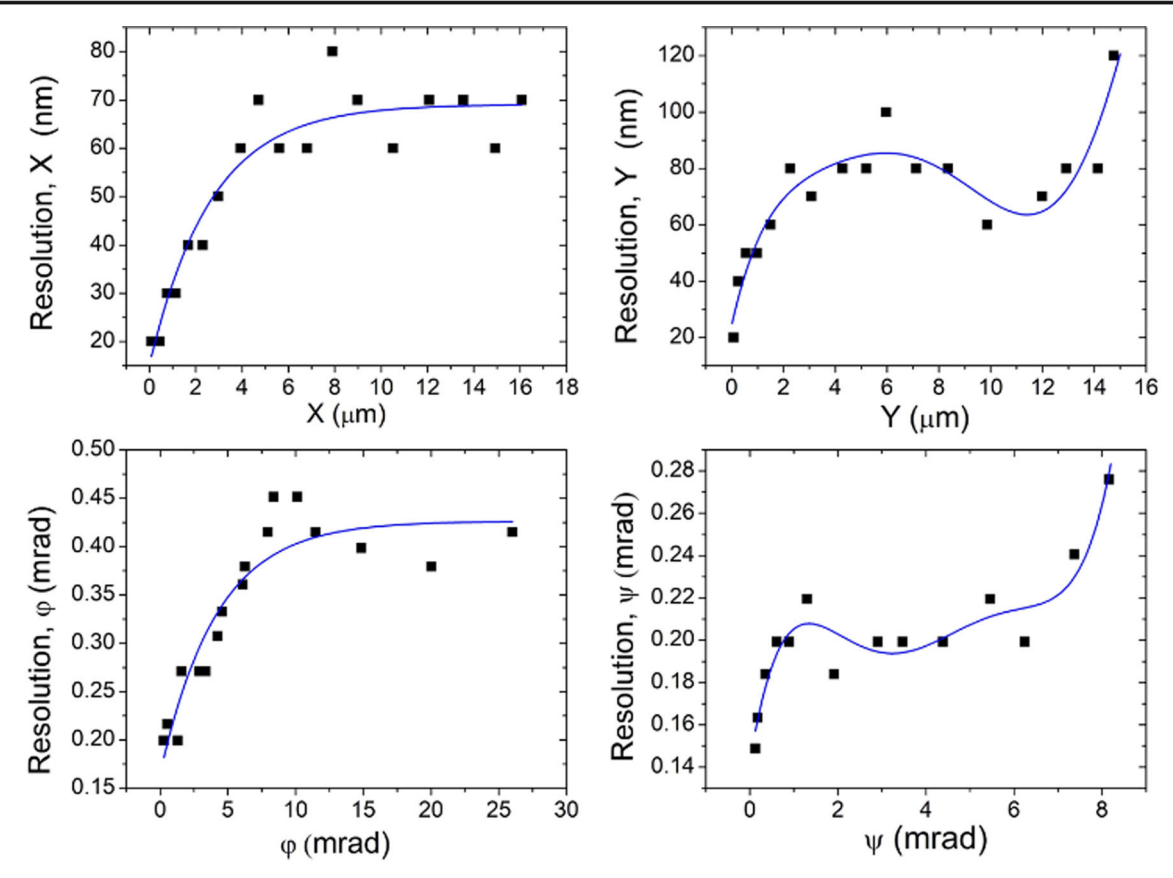


Fig. 10 Resolution variation along four DOFs

due to the differences in the design of both structures, not a disagreement. It must be noted that the total variation in resolution measurements is 100 nm (Y) over 15  $\mu$ m, which is 0.7% of maximum displacement (Fig. 10).

### 6.2 Repeatability measurement experiment

Repeatability is the variation in the end-effector position over attempts to produce the same outcome under the similar experimental conditions, in our case displacing sAFAM's arm to the same position under the same actuator voltages (bias). Repeatability was determined by running number of actuation cycles at 4 Hz with a constant actuation voltage for a specific actuator, and for different magnitude of the deflection. This allows to determine changes in the initial and final positions of the robotic arm after each cycle. Repeatability is derived from error variance between the initial-final points for specific number of the cycles. Applying this method, it was determined that repeatability ranges between 20 and 150 nm for X and Y translation, and between 0.15-0.26 mrad for  $\varphi$  and  $\psi$ .

Figure 11 illustrates variation of the repeatability depending on the deflection magnitude of the sAFAM arm in X, Y, pitch, and yaw. As in case of the resolution measurements, best for repeatability of the sAFAM structure is at lower magnitudes of deflection (actuation voltage). For the X and Y directions, there

is a distinguishable plateau for the displacements above 8  $\mu$ m, where repeatability ranges between 100 and 110 nm in Y direction and 110–150 nm in X. That is the case for the pitch and yaw angle as well, where plateau is above 5 mrad for pitch angle ( $\phi$ ) and 1 mrad for yaw angle ( $\psi$ ).

### 7 Conclusion and future work

In this paper we propose sAFAM, a novel 3D-assembled microrobot with four degrees of freedom. The microrobot was first simulated using Finite Element (FEA) analysis to dimensionally size the spring coupler design in the arm assembly. Simulation results indicated a workspace of 13 μm × 47 μm × 115 μm. The microrobot components were then fabricated on an SOI wafer with 100 µm thick device layer, then released and assembled using a custom passive microgripper mounted on a robotic assembly station. The overall dimensions of the assembled sAFAM microrobot are 10 mm by 10 mm by 1.5 mm, while its measured workspace was  $16 \mu m \times 20 \mu m \times 118 \mu m$ . Thus, simulation results using Finite Elements are consistent with the experimental results obtained using stereo images acquired from a highresolution microscope imaging system.



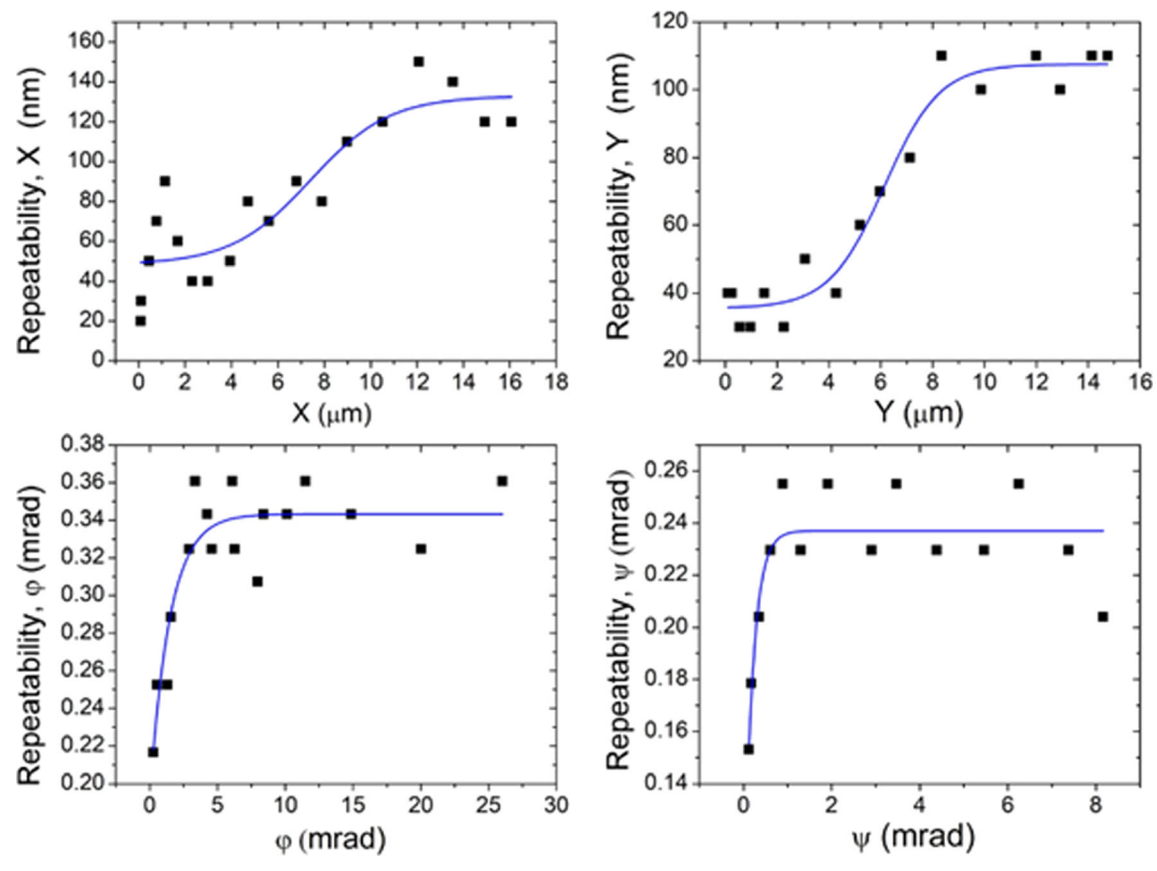


Fig. 11 Repeatability variation along four DOFs

Precision evaluation of the proposed sAFAM structure with a laser displacement sensor further indicates that microrobot's best resolution is 20 nm. Resolution coupled with the best result for the repeatability of 20 nm, makes the sAFAM suitable for applications at sub-micron and nanoscale. Due to the fact that the sensor we employed to measure resolution had a precision of 10 nm, we expect that resolution and repeatability of the sAFAM may be below this value. Furthermore, the measured decrease of resolution and repeatability at specific locations in the workspace could be due to nonlinear buckling effects in the thermal actuators, and amplification of fabrication errors on the two springs.

Future work includes changes in the design of the thin beam springs for the improvement of coupling between the actuators and sAFAM arm illustrated in this work; changes in the design of the actuator bank to produce even higher driving forces and avoid buckling at large voltages. Structural fatigue of an assembled sAFAM will be studied with repeated actuation test to evaluate assembly and structural reliability. An increased Zyvex connector stiffness will be studied in conjunction with new bonding materials, and automation of the assembly processes is being pursued. We will also conduct in-situ SEM characterization of the sAFAM, together with micro/

nanoprobing and handling tasks, and experimental characterization of reliability after repeated actuation cycles.

**Acknowledgements** This work was supported by National Science Foundation Grants #IIS 1633119 and #CMMI 1734383. We wish to thank the Micro Nano Technology Center (MNTC) staff at the University of Louisville, for their help with cleanroom fabrication.

### References

- Floyd S, Pawashe C and Sitti M (2009) "Microparticle Manipulation using Multiple Untethered Magnetic Micro-Robots on an Electrostatic Surface. in *The* 2009 *IEEE/RSJ International* Conference on Intelligent Robots and Systems, St. Louis, USA
- Floyd S, Pawashe C, Sitti M (2009) Two-dimensional contact and noncontact micromanipulation in liquid using an untethered Mobile magnetic microrobot. IEEE Trans Robot 25(6):1332–1342
- Jeon S, Jang G, Choi H, Park S (2010) Magnetic navigation system with gradient and uniform saddle coils for the wireless manipulation of micro-robots in human blood vessels. IEEE Trans Magn 46(6):1943–1946
- Donald BR, Levey CG, McGray CD, Paprotny I, Rus D (2006) An Untethered, Electrostatic, Globally controllable MEMS micro-robot. J Microelectromech Syst 15(1):1–15
- Karagozler ME, Thaker A, Goldstein SC and Ricketts DS (2011)
   "Electrostatic Actuation and Control of Micro Robots Using a Post-Processed High-Voltage SOI CMOS Chip. in 2011 IEEE



- International Symposium of Circuits and Systems (ISCAS), Rio de Janeiro, Brazil
- Basset P, Buchaillot L, Kaiser A and Collard D (2001) "Design of an autonomous micro robot. in ETFA 2001. 8th International Conference on Emerging Technologies and Factory Automation. Proceedings (Cat. No.01TH8597), Antibes-Juan les Pins, France, 15–18
- Tang Y, Chen C, Khaligh A, Penskiy I, Bergbreiter S (2013) An Ultracompact dual-stage converter for driving electrostatic actuators in Mobile microrobots. IEEE Trans Power Electron 29(6): 2991–3000, 16 July
- Khamesee MB, Kato N, Nomura Y, Nakamura T (2002) Design and control of a microrobotic system using magnetic levitation. IEEE/ASME Transactions on Mechatronics 7(1):1–14
- Diller E, Floyd S, Pawashe C, Sitti M (2012) Control of multiple heterogeneous magnetic microrobots in two dimensions on nonspecialized surfaces. IEEE Trans Robot 28(1):172–182
- Hsu A, Cowan C, Chu W, McCoy B, Wong-Foy A, Pelrine R, Velez C, Arnold D, Lake J, Ballard J and Randall J (2017) Automated 2D micro-assembly using diamagnetically levitated milli-robots. In 2017 International Conference on Manipulation, Automation and Robotics at Small Scales (MARSS), Montreal
- Yeh R, Kruglick EJJ and Pister KSJ (1995) "Microelectromechanical components for articulated microrobots. in The 8th international conference on solid-StateSensors and actuators, and EurosensorsIX, Stockholm, Sweden
- Sarkar N, Stratheam D, Lee G, Olfat M and Mansour RR (2017) "A
  platform technology for metrology, manipulation and automation at
  the nanoscale. In 2017 International Conference on Manipulation,
  Automation and Robotics at Small Scales (MARSS), Montreal
- Murthy R, Das AN and Popa DO (2008) ARRIpede: an assembled micro crawler. In 8th IEEE Conference on Nanotechnology, 2008. NANO '08, Arlington, TX
- Murthy R, Das A and Popa DO (2008) ARRIpede: a stick-slip micro crawler/conveyor robot constructed via 2 ½D MEMS assembly. in IEEE/RSJ international conference on intelligent robots and systems, 2008. IROS 2008, Nice, France
- Tsui K and Geisberger A, "Sockets for microassembly". United States patent US7025619B2, 13 2 2004

- Geisberger A, Skidmore G and Tsui K, "Microconnectors and nonpowered microassembly therewith". United States patent EP1564183A2, 13 2 2004
- Murthy R, Stephanou HE, Popa DO (2013) AFAM: an articulated four axes microrobot for nanoscale applications. IEEE Trans Autom Sci Eng 10(2):276–284
- Tsang PH, Li G, Brun YV, Freund LB, Tang JX (2006) Adhesion of single bacterial cells in the micronewton range. PNAS 103(15): 5764–5768
- Achanta S, Drees D, Celis J-P (2007) Investigation of friction on hard homogeneous coatings during reciprocating tests at micro-Newton normal forces. Wear 263(7–12):1390–1396
- Whittaker JD, Ethan MD, Tanenbaum DM, McEuen PL, Davis RC (2006) Measurement of the adhesion force between carbon nanotubes and a silicon dioxide substrate. Nano Lett 6(5):953–957
- Yang Z and Popa DO (2018) "A general kinematic modeling framework for a 3D compliant micromechanism. in *International Conference on Manipulation, Automation and Robotics at Small Scales*, Nagoya, Japan
- Das AN, Zhang P, Lee WH, Popa D and Stephanou H (2007) "μ3: multiscale, deterministic micro-Nano assembly system for construction of on-wafer microrobots. in Proceedings 2007 *IEEE International Conference on Robotics and Automation*, Roma, Italy
- Que L, Jae-Sung P, Gianchandani YB (2001) Bent-beam electrothermal actuators-part I: single beam and cascaded devices. J Microelectromech Syst 10(2):247–254
- Park J-S, Chu LL, Oliver AD, Gianchandani YB (2001) Bent-beam electrothermal actuators-part II: linear and rotary microengines. J Microelectromech Syst 10(2):255–262
- Cragun R, Howell LL (1999) Linear thermomechanical microactuators. ASME - MEMS 1:181–188
- Maloney JM, Schreiber DS, De Voe DL (2004) Large-force electrothermal linear micromotors. J Micromech Microeng 14(2):226–234
- Madou MJ (2002) Fundamentals of microfabrication the science of miniaturization. CRC Press
- Hopcroft MA, Nix WD, Kenny TW (2010) What is the Young's Modulus of silicon? J Microelectromech Syst 19(2):229–238

**Publisher's note** Springer Nature remains neutral with regard to jurisdictional claims in published maps and institutional affiliations.

